Analysis of mechanical behavior of 3D printed heterogeneous particle-polymer composites

Erina Baynojir Joyee, Lu Lu, Yayue Pan [*]

Department of Mechanical & Industrial Engineering, University of Illinois at Chicago, Chicago, IL, 60607, USA

ARTICLE INFO

ABSTRACT

Additive manufacturing has emerged as a powerful tool for fabrication of heterogeneous particle-polymer composites with enhanced material properties. These synthetic particle-polymer composites are lightweight, tough and showcase remarkable fracture toughness. Yet there is still a big knowledge gap in engineering particle microstructure orientation and loading fraction, to achieve the desired stress-deformation behavior of particle-polymer composites. To close this knowledge gap, it is essential to study the fracture toughness and stress-deformation patterns. Hence, in this paper, we additively manufactured particle-polymer composites with varied particle chain distributions and particle loading fractions, and investigated the mechanical behaviors of those composites both experimentally and analytically. Additionally, we investigated the influence of layer thickness on the Young's modulus and breaking propagation paths of the 3D printed samples. It is observed that the breaking edges remain smooth for parts printed with a small layer thickness and becomes irregular with asymmetrical fractures as the layer thickness is bigger than a critical value. The Young's modulus predicted by Cox-Krenchel model show similar trends as in the experimental results and validates the feasibility of the models in guiding the design of particle distribution, orientation and concentration in heterogeneous particle-polymer composites. Yet a higher modulus is predicted when particle chains are aligned parallel to the force direction, while a much smaller modulus, as small as the modulus of pure polymer, is predicted when particle chains are aligned perpendicular to the force direction. The analytical results of S1-0 and S1-45 composites agree with the experimental results with a deviation of 5.5%. While the analytical results of S1-90 do not agree with the experimental results, mainly due to the weak interfacial bonding between particle chain and polymer in the 3D printed composites. Both analytical and experimental results show that the particle-polymer composites with high particle volume loading fraction and parallel particle chain orientation has the highest stiffness.

1. Introduction

Biological organisms in nature often showcase remarkable structure designs with sophisticated and complex filler embedding patterns [1]. These naturally evolved composites feature complex architecture with various distribution, orientation, and concentration of reinforcing particles including spherical particles, pellets, and fibers. Some examples are the claws of lobster and crabs, dactyl clubs of peacock mantis shrimps, beetle wings and gigas fish scales [2–5]. These types of biological architectures have inspired researchers to design the next-generation structural heterogeneous particle-polymer composite, which is characterized by locally controlled material distribution and hence localized properties. The particle loading fraction, orientation, and dispersion in the polymer matrix have a significant effect on the overall tensile strength, elasticity and stiffness of the heterogeneous composite material. Various potential applications can be possible with this kind of new material, including controlled drug delivery systems, diagnostic medicine, biomimetic devices, and actuating and sensing components [6,7].

Traditionally, researchers have combined conventional manufacturing process and complex chemical preprocess to fabricate particle-polymer composites. Some examples include injection and compression molding, CNC machining, filament winding, prepreg method, resin film infusion, etc. [8–11]. Some major drawbacks of these techniques are time consuming, requiring manual assembly, limited heterogeneity in the fabricated composite, and limited of design

---

freedom. In recent years, additive manufacturing (AM) has emerged as an effective way for fabricating different types of heterogeneous particle-polymer composites with complicated architectures [6,7, 12–16]. Despite those advances, mechanical and fracture properties of the resultant materials are still not well known.

In the past decades, numerous researches have been conducted to study the mechanical properties of both the homogeneous and heterogeneous particle-polymer composites [17–19]. Most studies primarily investigated the change of shear modulus and stress, with different dispersion and orientation of the filler [2,17,20,21]. Some studies investigated elastic modulus of composites and compared with the neat polymer [21–28]. It was observed that the polymer elasticity and maximum strain capability increase with parallel filler alignment [27, 29,30]. Various experiments were conducted to investigate the change of mechanical properties with respect to the aspect ratio of filler [31], filler-polymer compatibility, and interfacial interaction of different aligned fillers such as carbon nanotubes (CNTs), multiwalled carbon nanotubes (MWCNT), alumina platelets [2,18–21,32], and, glass fibers [33,34]. Besides, the mechanical properties of particle-polymer composites were modeled and simulated [27,35–41]. For example, Kalina et al. [42] modeled the deformation dependent mechanical behavior of chain-like micro-composites and compared their numerical simulation results with established experimental studies [20]. A strong relationship between sample interfacial geometries and the applied mechanical preloads was demonstrated in their study.

Despite the extensive research on mechanical properties of heterogeneous polymer composites, most of the studies focused on composites fabricated by traditional manufacturing techniques. Few studies explored 3D printed composites. A wide range of research studies were reported on additive manufacturing techniques for fabricating composites with customized assembly and distribution of spherical particles [6,21,31]. However, most of the current mechanical behavior studies focused on polymer composites with fiber or platelet filler materials or carbon nanofibers, while little is known about composites constructed by assembled spherical particles. So, there is an urgent need for closing the knowledge gap of the material properties of 3D printed heterogeneous polymer composites composed of spherical particle assemblies.

To address the above knowledge gap, this study fabricates heterogeneous polymer composite specimens by assembling iron oxide spherical particles in liquid resin and curing the particle assembly in resin through a layer-by-layer vat photopolymerization technique. Then the stress-strain behaviors of the printed composites are characterized. Several modes of the stress-strain behavior, such as elasticity and plasticity are analyzed and correlated to the particle chain orientations and concentrations. Moreover, this study also explores how the 3D printing layer thickness setting impacts mechanical properties such as Young's modulus and breaking propagation path. The rest of the article is arranged in the following order: Section 2 describes material and characterization methods, characterizes curing sizes, discusses the fabrication of samples, and models the Young's modulus. Section 3 analyzes the modeling results and experimental data. Mechanical test results and interfaces are also discussed. A summary of the research work is presented in section 4.

2. Material and method

2.1. Material

In this study, synthetic black iron oxide spherical particles purchased from Alpha Chemical (Missouri, USA) were used as the composite filler material. The average diameter of spherical iron oxide particles is about 300 nm with a specific surface area of $7.0 \, m^2/g$. Spot E photocurable polymer resin purchased from Spot-A Materials (Barcelona, Spain) was used as the base material. Its light-yellow color makes it easy to observe the iron oxide particles in it both before and after 3D printing. The photo-cured Spot E resin demonstrates exceptional toughness, which

makes it the perfect material for applications needing soft yet resilient rubbery materials such as bio-inspired soft robotics [43]. It also provides up to 65% elongation behavior and a low viscosity for effortless material recovery, cleaning and manipulation without any volatile organic compound (VOC) inside.

Suspensions were prepared by mixing resin and iron oxide particles with Thinky AR-100 mixer (THINKY CORPORATION, Tokyo, Japan). The mixer was run for about 3–5 min until the homogeneous phase was achieved. To study the mechanical behavior of the composites, particle-polymer suspension was prepared with particle volume loading fractions ranging from 4.5% to 9.5%. From literature [6,7,31] and our own experience, we observed that the volume fraction of iron oxide particles less than 4.5% had negligible effect on the polymer mechanical and functional properties. In case of particle volume loading fractions higher than 9.5%, the curing time increased significantly due to the light absorption by the dark colored filler particles [6,7]. This significant increase in curing time would lead to manufacturing failures and instabilities. Hence, in this study, we defined our research scope on composites 3D printed by using feedstocks only with low filler loading fractions. However, it is noteworthy that although the overall loading fraction of the feedstock used our study is as low as 9.5%, after the particle assembly, the local particle loading fraction in polymer matrix of the printed composite can be as high as 70% [6,7]. Due to the particle assembly effect, simply increasing the overall loading fraction has limited effects on both the local loading fraction of assembled particle patterns and the printed composite properties, yet significantly increases the manufacturing expenses. Therefore, in this study, with the research focus of particle assembly effects on composite mechanical properties, we perform experiments on composites fabricated out of suspensions with an overall particle loading fraction in the range of 4.5%–9.5%.

2.2. Experimental setup and M-PSL process

Recently, a few 3D printing techniques have been developed for production of heterogeneous particle-polymer composites [2,6,15,19, 44]. In our previous work, a 3D printing technology named magnetic field-assisted projection stereolithography (M-PSL) has been developed for 3D printing of smart particle-polymer composites with locally controlled particle distribution, assembly, and orientation [6]. This paper used this M-PSL technique developed in our previous study to fabricate heterogeneous particle-polymer composites. Fig. 1 illustrates the M-PSL setup used to print the particle-polymer composite samples in this study. The M-PSL setup is a bottom-up projection stereo-lithography system integrated with an external magnetic field generation system, consisting of a resin vat, an imaging unit, movable permanent magnets, platform, and linear stages, as shown in Fig. 1(b). During the printing process, the orientation of the reinforcing filler particle chains is finely tuned within each layer by using the permanent magnets.

The M-PSL process begins with developing a digital computer model of the object, which is then sliced into a set of 2D cross section layers. Each sliced layer is converted to digital masks and then sent to the imaging unit. The imaging unit projects patterned light for each slice, selectively exposing and hardening the resin. A layer of the resin is thus cured into a shape defined by the corresponding light pattern. To print a layer of particle-polymer composite, before the light curing, the permanent magnets are moved or placed properly to form external magnetic fields, to assemble magnetic particles into chains with desired dimensions and alignments. This whole process is repeated until the last layer to fabricate the designed particle-polymer composite model.

2.3. Material characterization

As illustrated in Fig. 2(a), in the M-PSL printing process, before light curing, the particle is initially dispersed in the liquid resin which in turn affects the photo-polymerization significantly. The curing shape, including width and depth, will be affected by the particle distributions.
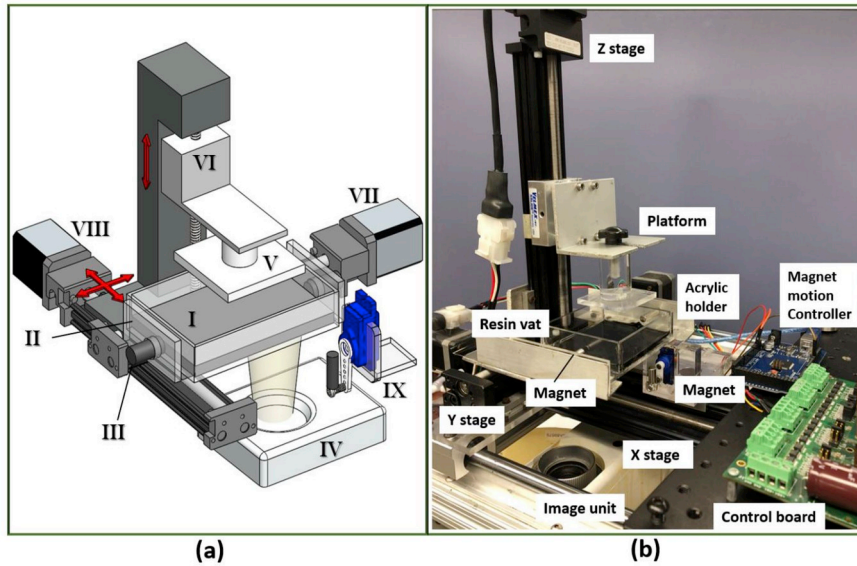
Fig. 1. (a) A schematic diagram of the heterogenous particle-polymer composites printing system using M-PSL process. (I) Resin vat (II) acrylic holder (III) permanent magnet (IV) image unit (V) platform (VI) Z stage (VII) Y stage (VIII) X stage (IX) rotational magnet, (b) A M-PSL prototype built in this work.
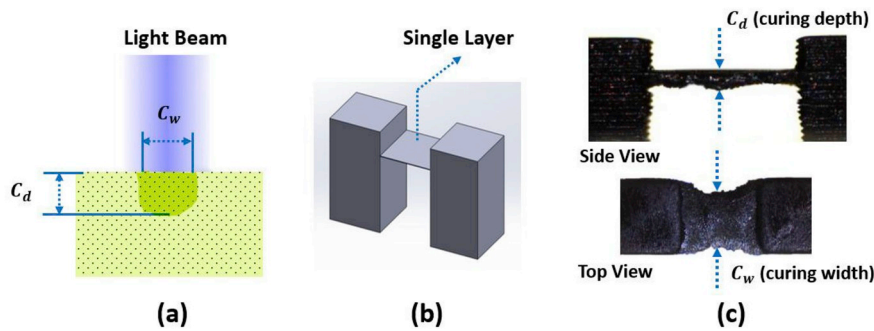

Fig. 2. (a) Schematic diagram of photo-curing, where C_d is curing depth and C_w is curing width, (b) CAD design of a bridge model for curing calibration study, and (c) Experimental calibration of curing depth and curing width.

To 3D print particle-polymer composites precisely with desired material properties using the M-PSL technology, it is essential to analyze the effect of iron oxide particles on curing properties of the particle-polymer suspensions and identify the appropriate curing process settings for manufacturing. In this study, the curing depth and width of particle-polymer suspensions are characterized and modeled with varied particle volume loading fractions. As shown in Fig. 2(b) and (c), a bridge model is printed with seven different iron oxide particle volume loading fractions. The center thickness and width of the overhanging cured layer in the bridge model are measured under the microscope. The measured thickness and width are then taken as the experimental curing depth C_d and curing width C_w of the particle-polymer suspension with that particle volume loading fraction respectively. Four replication experiments are performed for each particle volume loading fraction. The exposure time t used in all experiments is 30 s.

In our previous study [7], the curing depth was modeled using a modified version of ceramic-suspension curing model proposed by Griffith and Halloran [45]:

$$C_d = \left(\frac{n_0}{n_p - n_0}\right)^2 \frac{\lambda^2}{d} ln\left(\frac{t}{t_c}\right) \frac{1}{\varphi} \qquad (1)$$

where $??$ is the average diameter of particles, φ is the particle volume loading fraction in the polymer, t is the exposure time, t_c is the critical exposure time, $??$ is the light wavelength, and n_0 and n_p are refractive

indexes of the resin and particle, respectively. The critical exposure time for each volume fraction was experimentally measured and found to be ranging from 3.1 s to 10.5 s. The details of this experimental procedure to find critical exposure time are described in our previous publications [46,47]. The refractive index of resin and iron oxide spherical particles is 1.4 and 2.35, respectively [48]. The effective light wavelength is 380–480 nm and the average diameter of particles is 300 nm.

Fig. 3(a) plots the experimental curing depth of particle-polymer composites versus the particle volume loading fraction. It shows that, the curing depth decreases in a nonlinear trend as the particle volume loading fraction increases. From Fig. 3(b), we can observe that the experimental curing depth matches closely with the values predicted by Eq. (1). The average prediction error for those seven samples is 13.25%.

The relationships of curing width (C_w) with beam profile and refractive index are established in Refs. [49–51],

$$C_w \propto \left(\frac{n_0}{\Delta n}\right)^2 \times \frac{\lambda^2}{d} \times \sqrt{ln\left(\frac{t}{\varphi.t_c}\right)} \qquad (2)$$

where $\Delta n = n_p - n_0$. Using a constant F to represent $\left(\frac{n_0}{\Delta n}\right)^2 \times \frac{\lambda^2}{d}$ and rewriting Eq. (2), we can obtain:

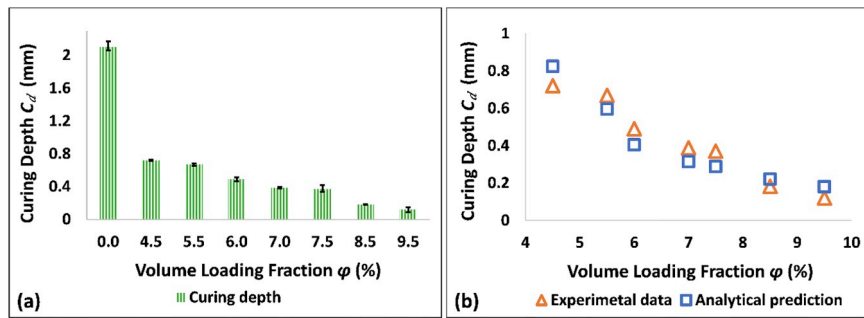$$C_w \propto F \times \sqrt{ln\left(\frac{t}{\varphi.t_c}\right)} \qquad (3)$$

Fig. 3. (a) Experimental curing depth at varying volume loading fractions of magnetic particles, (b) Comparison of the experimental and analytical curing depth.

where F is a function of the beam profile, refractive index and particle diameter. We can simply modify Eq. (3) by adding a slope and intercept as below:

$$C_w = k \times F \times \sqrt{ln\left(\frac{t}{\varphi.t_c}\right)} + C = 0.62 \times F \times \sqrt{ln\left(\frac{t}{\varphi.t_c}\right)} - 0.71 \quad (4)$$

Here, k and C are parameters that can be fitted experimentally. To validate this curing width model, we measured the curing width of samples with loading fractions of 4.5%, 6.0%, 7.5% and 9.5%, and calculated the fitted values of k and C, which are 0.62 and −0.71, respectively. The fitted model in Eq. (4) is then validated by experimental measurements of samples with loading fractions of 5.5%, 7.0%, and 8.5%, as shown in Fig. 4. The average prediction error is only 3.64%. It is verified that accurate predictions of curing width for suspensions with varied particle volume loading fractions can be obtained using the fitted model in Eq. (4).

2.4. Composite samples printed by M-PSL

To study the effect of material composition heterogeneity on composite properties, two sample groups are designed and printed using the M-PSL process. The key M-PSL process parameter, curing time, for varied layer thickness and particle loading fractions is determined according to the study in 2.3. The first group of the composite samples, Sample 0 (S0), as illustrated in Fig. 5(a), has non-structured magnetic particles uniformly distributed in the polymer matrix. The second group of samples is named as Sample 1 (S1) which has oriented magnetic particle chains uniformly distributed in the polymer matrix, as illustrated in Fig. 5(d). For fabricating S1, a uniform magnetic field with a magnitude of 1276 A/m is applied to assemble particles into the desired chain architecture.
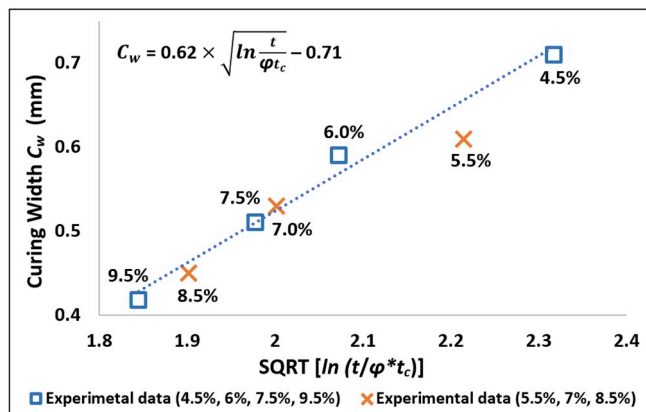

Fig. 4. Curing width (C_W) vs *SQRT* [ln (t/φ*t_c)], where *SQRT* denotes square root function, t is the exposure time, t_c is the critical exposure time and φ is the particle volume loading fraction in the polymer.

Once particles are assembled and aligned, the structured particle-polymer suspension is exposed to light and selectively polymerized to form a layer. This process repeats until the last layer is printed. The printed part is then rinsed in ethyl alcohol to remove any uncured resin on the printed sample. After that, the samples are post-cured in an ultraviolet chamber to relieve residual stresses on the surface of printed samples caused by the photo-polymerization process. Fig. 5(b) shows a printed S0 specimen with a 4.5% volume loading fraction. Sample S0 specimens with varied volume loading fractions are printed without the presence of magnetic field. From the microscopic image in Fig. 5(c), the iron oxide particles can be seen uniformly distributed inside the composite. Fig. 5(d) illustrates sample S1 design which has particle chain structures embedded in polymer matrix. An S1 specimen with a 4.5% volume loading fraction is showed in Fig. 5(e) and (f). From Fig. 5(f), the chain-like particle structures can be clearly observed in the printed sample.

The microstructures of particle distribution in polymer matrix are observed from a scanning electron microscope (SEM). The SEM images are recorded using a JEOL JSM-6320F (CA, USA) electron microscope operated at 3 kV. Fig. 5(g) shows SEM images of S0 where the spherical iron oxide particles are uniformly distributed in the polymer. The particles can be seen embedded in the polymer with a thin polymer coating around each particle. Fig. 5(h) shows SEM images of S1 with varied loading fractions, ranging from 4.5% to 9.5%. It gives a closer look at the microscale particle chain structures embedded in the polymer. The chains are aligned unidirectionally along the magnetic flux. With increasing loading fraction, the chain width increases due to the denser particle distribution.

2.5. Modeling of Young's modulus

To investigate the Young's modulus of the 3D printed composite analytically, the following assumptions were made: i) matrix is void free; ii) the particle-polymer composite is initially in a strain-free state; and iii) the polymer acts as linearly elastic materials. With these assumption, the Young's modulus of the particle-polymer composite (Y_C) and its relation with volume loading fraction of filler particles (φ_i) can be modeled using a Cox-Krenchel model with Carman-Reifsnider correction [52]:

$$Y_C = Y_i \eta_0 \eta_l \varphi_i + (1 - \varphi_i) Y_m \quad (5)$$

where, Y_C, Y_i, and Y_m are the elastic moduli of particle-polymer composite, iron oxide particle, and pure polymer, respectively. φ_i is the volume loading fraction of iron oxide particle in the composite. The theoretical values of Y_i and Y_m are previously known as 214 GPa and 12 MPa, respectively, from the literature [53]. η_0 is the Krenchel orientation factor [52] which is defined as l when particles are aligned parallel to the stress and 0 for transverse alignment, with all other values falling in the range of 0–1 for different orientation angles. η_l is the Cox fiber-length efficiency factor which is defined in Ref. [52] as,
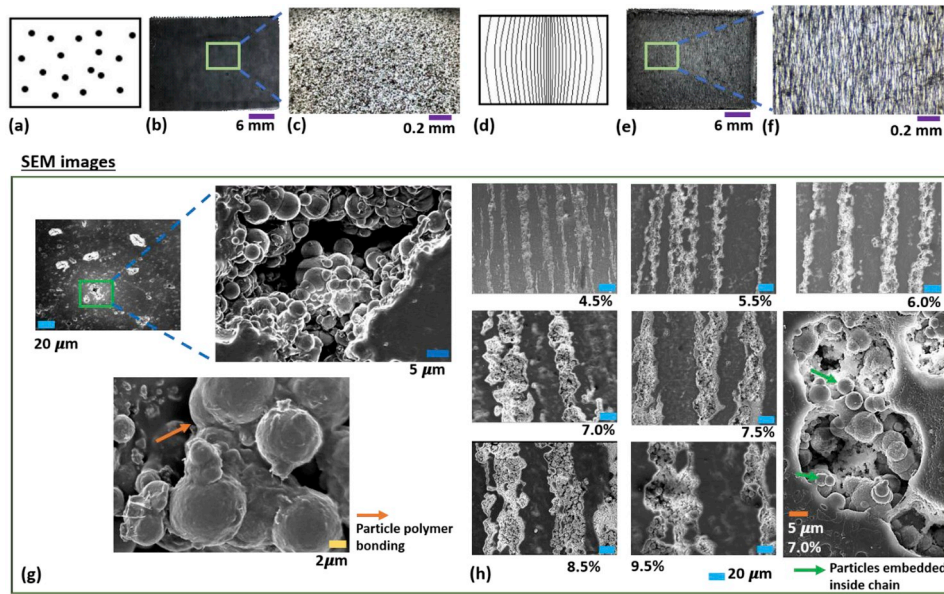
Fig. 5. (a, d) Schematic diagrams, (b, e) Photos of printed parts and (c, f) Microscopic images of S0 and S1 respectively, (g) SEM images of sample S0, (h) SEM images of sample S1 with varied loading fractions.

$$\eta_l = 1 - \frac{tanh\left(\beta \frac{L}{d}\right)}{\beta \frac{L}{d}} \tag{6}$$

where,

$$\beta = \sqrt{\left(\frac{-3Y_m}{2Y_i \ln\varphi_i}\right)} \tag{7}$$

L and d are the length and width of particle chain. The value of fiber length efficiency factor η_l approaches 1 for fillers with high aspect ratio. Previous studies have reported that η_l approaches 1 as L/d > 10 which underlines the fact that high aspect ratio particle fillers are preferred [52]. In our study, these physical parameters (L, d) are directly measured from SEM images of the particle assembly.

2.6. Tensile test experiment design

To validate the analytical model, experiments were performed to measure the mechanical properties of fabricated parts with varied iron oxide particle volume loading fractions and particle assembly orientations. The Young's modulus of S0 and S1 sample specimens are measured using an Instron 3360-series (Instron, Norwood, MA) device at room temperature and an extension rate of 5 mm/min. To investigate the effect of particle chain orientation on mechanical properties of printed samples, three orientations are tested in case of S1: parallel (S1-0), at an angle of 45° (S1-45), and perpendicular (S1-90) to the applied tensile load. As shown in Fig. 6, S1-0 illustrates the test setup where the particle chain structures are parallel to the tensile force, while the S1-45 setup places the chain structures at a 45° angle to the tensile force and the S1-90 setup places the chain structures perpendicular to the tensile force.

3. Result and discussion

3.1. The effects of particle chain orientation

A comparison of measured Young's modulus for the pure resin and S1 samples with varied particle chain orientations (S1-0, S1-45, and S1-90) is shown in Fig. 7, together with the corresponding analytical predictions of Y_c calculated by Eq. (5). The printed sample used for Fig. 7
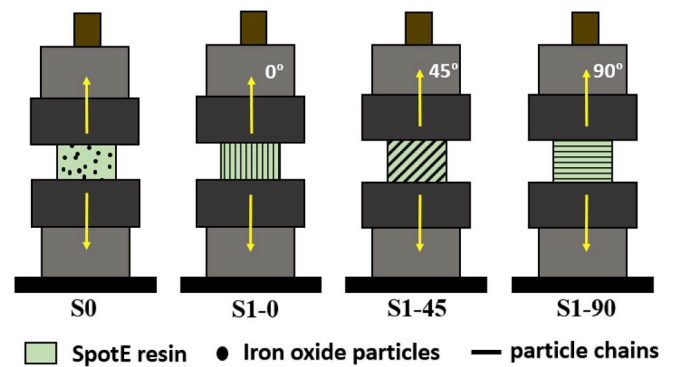

Fig. 6. Schematic diagram of S0 and S1 samples during tensile test.

had a layer thickness of 100 μm.

As shown in Fig. 7, in the experimental measurements, a higher Young's modulus is observed in S1 samples, compared to the modulus of pure resin. A strong correlation of the Young's modulus with the particle chain orientation was observed. Composites with particle chains
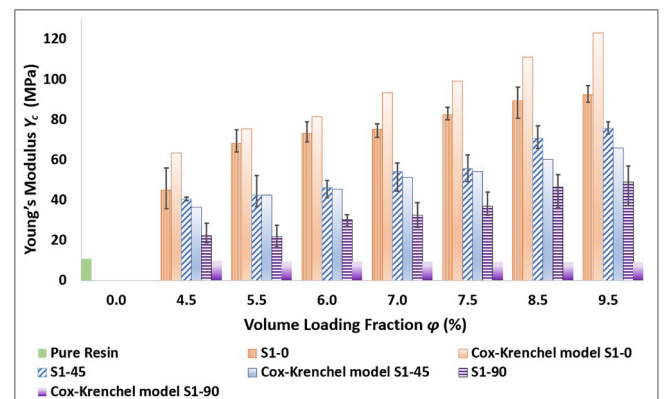

Fig. 7. Comparison of Young's modulus (experimental and predicted) among printed parts made by using the pure resin and composites of resin with aligned iron oxide particles.

oriented along the tensile force direction showed a higher modulus than the ones with other particle chain orientations. The lowest Young's modulus of S1 specimen was measured to be 22 MPa, when the particle chain orientation is 90° and the particle loading fraction is the lowest (S1-90, $\varphi = 4.5\%$). With a parallel particle chain orientation, S1-0 samples showed the highest Young's modulus: about 45 MPa with a 4.5% volume fraction and 92 MPa with a 9.5% volume fraction of particles. As shown in Fig. 7, the modulus decreases as the angle of particle orientation increases. An approximately linear increase of Young's modulus (Y_c) can be observed with the increase of volume loading fraction. Both the predicted and experimental Y_c values show a linear relation with the increasing loading fraction.

Overall differences between the experimental and analytical Y_c are observed in Fig. 7, because the analytical model assumes perfect assembly of spherical particles with strong bonding strength between particles, and perfect interfacial bond between filler assembly and resin. For samples with particle chains oriented along the tensile force direction (S1-0), the Y_c values predicted by Cox-Krenchel model are comparatively higher than the experimental values. It can be explained by the definition of Cox fiber-length efficiency factor η_l in the model. The model was developed to predict the modulus of fiber-polymer composites, instead of particle chain-polymer composites, and η_l is a function of the fiber length and width, as introduced in Eq. (6). In this study, we redefined η_l as a function of particle chain length and width, to use Cox-Krenchel model for understanding the 3D printed particle chain-polymer composites. Yet the particle chain assembly does not have the same stiffness as fibers along the length direction, making the actual length efficiency factor smaller and thus the actual modulus smaller than the modeled value. Fig. 7 shows that differences between the experimental and Cox-Krenchel model predicted Young's modulus becomes smaller by increasing the angle between particle chain direction and tensile loading direction from 0° (S1-0) to 45° (S1-45). The modeled Young's modulus of S1-0 and S1-45 composites agree with the experimental results with a deviation of ~5.5%.

However, the analytical results of Young's modulus of S1-90 do not agree with the experimental results. For S1-90 samples in which the particle chains are aligned perpendicular to the load, in the Cox-Krenchel model, the influence of Young's modulus of fiber (Y_i) on the composite becomes negligible as the Krenchel orientation factor η_0 becomes zero, making the predicted Y_c close to the experimental modulus of pure polymer. However, this assumes perfect bonding between fiber and polymer matrix, which is not the case in the particle chain-polymer composites which are 3D printed in a layer-by-layer fashion in this study. First, the chain assembled by spherical particles are not aligned as perfectly as fibers. Additionally, as there is no surface modification of

iron oxide particle fillers, the interface bonding between particle chain and polymer matrix is weak, resulting in a break in the particle chain-polymer interface at an early stage in the experiments, hence a bigger experimental modulus.

The tensile strength of S0 and S1 samples with a volume fraction varying from 4.5% to 9.5% are measured and plotted in Fig. 8. It is observed that the ultimate tensile strength increases almost linearly as the filler volume loading fraction increases. This can be attributed to the rising stiffness in the specimens as the volume fraction of the filler increases. Another possible reason behind the efficient filler networking could be the interaction of the filler components with the polymer matrix [19]. We can also observe from Fig. 8(a) that the orientation of the particle chain structures has a significant impact on the tensile strength. Heterogeneous composite S1-0 samples which are characterized by embedded particle chain structures parallel to the tensile force, show the highest tensile strength compared to S0 and S1-90 composite samples.

Fig. 8(b) plots the maximum strain of S0 and S1 samples at break. It is observed that the strain at break decreases with increasing particle volume loading fraction. We can observe a higher strain at break of S0 compared to S1. In comparison, S1-0 has the smallest strain at break. This indicates that S0 has a higher elasticity than S1. In S1-0, the particle chains which align parallel to the applied force reinforces the composite fully while in the case of S1-90, the perpendicular particle chain alignment has the least reinforcement on the composite stiffness. Accordingly, S1-45 demonstrates elastic characteristics in between these two extremes, indicating a strong, but not linear correlation between the particle chain orientation and elastic properties.

3.2. Break propagation path analysis

The measured stress-strain curves and recorded break propagation processes for samples in groups S0 and S1 at varied particle volume loading fractions and particle chain orientations are shown in Fig. 9 (recorded video is in the Support material). Representative schematic diagrams and SEM images of the fracture surfaces are shown in Fig. 10, demonstrating the effects of particle chain orientation on the break propagation.

Supplementary video related to this article can be found at http s://doi.org/10.1016/j.compositesb.2019.05.051.

Based on the gradient of the stress-strain curve, curves have been partitioned to portions at points where there is either a sudden change in stress distribution or the direction of gradient changes with respect to the strain.

The first portion is identified before the first sudden change in stress (high positive gradient) and termed as relaxation period. As the loading
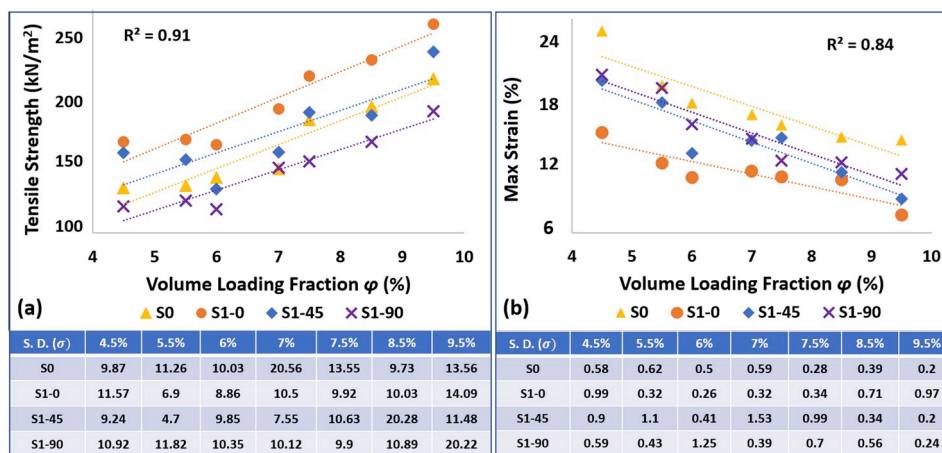

S. D. (σ)	4.5%	5.5%	6%	7%	7.5%	8.5%	9.5%
S0	9.87	11.26	10.03	20.56	13.55	9.73	13.56
S1-0	11.57	6.9	8.86	10.5	9.92	10.03	14.09
S1-45	9.24	4.7	9.85	7.55	10.63	20.28	11.48
S1-90	10.92	11.82	10.35	10.12	9.9	10.89	20.22

S. D. (σ)	4.5%	5.5%	6%	7%	7.5%	8.5%	9.5%
S0	0.58	0.62	0.5	0.59	0.28	0.39	0.2
S1-0	0.99	0.32	0.26	0.32	0.34	0.71	0.97
S1-45	0.9	1.1	0.41	1.53	0.99	0.34	0.2
S1-90	0.59	0.43	1.25	0.39	0.7	0.56	0.24

Fig. 8. (a) Tensile strength of S0 and S1 at different volume loading fractions, (b) Maximum strain of S0 and S1 at different volume loading fractions. The standard deviation at each point is given below the graphs.
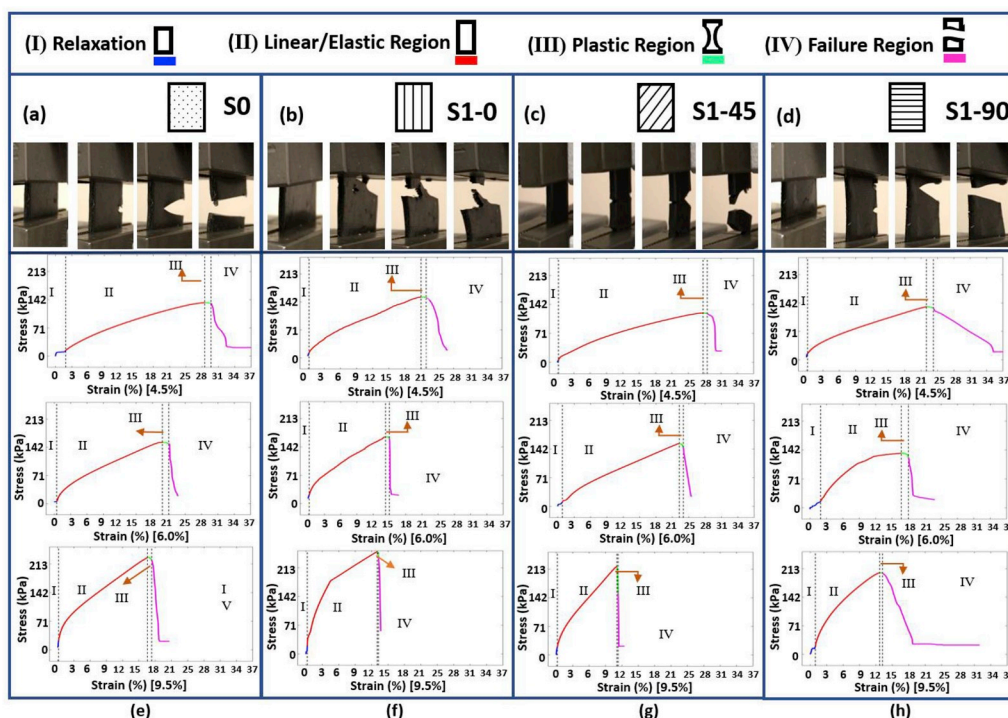
Fig. 9. (a–d) Breaking propagation of S0, S1-0, S1-45 and S1-90 respectively, (e–h) Stress-strain curves at varying volume loading fractions (4.5%, 6.0% and 9.5%) for S0, S1-0, S1-45 and S1-90, respectively.
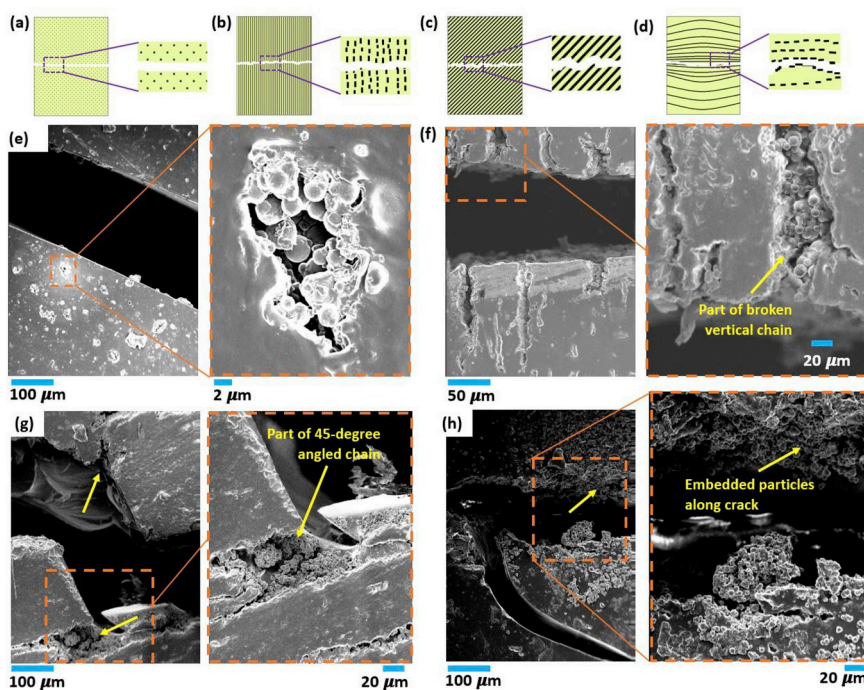

Fig. 10. Schematic diagrams of breaking edge for (a) S0, (b) S1-0, (c) S1-45, (d) S1-90 and SEM images of breaking edge for (e) S0, (f) S1-0, (g) S1-45 and (h) S1-90.

initiates, it affects the elastic properties provided by molecules of polymer interacting with the particles.

After the relaxation period, the elastic region can be observed, showing a gradual increase in stress with a constant increasing gradient. It is then followed by a comparatively shorter plastic region. We can observe extended plastic region in S0 and S1-90 from Fig. 9 (e) and (h). This is specially observed in lower volume loading fractions (i.e. 4.5%). However, for S1-0 and S1-45, we can barely observe the plastic region,

especially in high particle loading fraction (9.5%). For example, we see comparatively steeper plastic regions in the stress-strain curves in Fig. 9 (f) and (g). With increasing load, the composites finally reach the point of tensile failure where the adjacent chain molecules tear from each other. The tear normally follows a breaking propagation path. From the tensile tests, we can observe that the breaking propagation path is influenced by the distribution of filler and the orientation of particle chains.

The typical breaking path of S0 is shown in Fig. 10(a). The breaking path is linear and neat because of the homogeneous material composition in S0. The breaking pattern of particle-polymer composite samples S0 is found to be similar to the pattern observed in pure polymer samples. As shown in the SEM images in Fig. 10(a), the fracture surface is very smooth, implying a quick fracture which is also observed in the recorded tensile test video.

For S1-0 samples, the breaking is instantaneous and swift. The stress at break is the greatest in all samples. However, the fracture surface is not smooth, showing an irregular break propagation path. The breaking process and a SEM image of the fracture surface are shown in Figs. 9(b) and 10(b). We can observe that the break occurred in the weakest point of the particle chain where the chain length and width had comparatively smaller dimensions. The breaking surface was rough with asymmetrical fractures along the edge.

For S1-45, cracks are formed from the edge along the direction of particle chains and then break propagates. The breaking path was congruent with the angle of the particle chain. The breaking process and SEM image of S1-45 are shown in Figs. 9(c) and 10(c). From the SEM images, we can see that the breaking edge of the S1-45 is irregular and has particles embedded inside the chain.

Sample S1-90 forms multiple cracks from the edge along the direction of particle chains and then breaks by following the path of the chain structure. The breaking process and SEM image of S1-90 are shown in Figs. 9(d) and 11(d). From the SEM image, we can see that the crack is propagating along the chain orientation. We can also observe the broken chain and particles embedded in the chain.

3.3. The effects of 3D printing layer thickness

In 3D printed particle-polymer composite, printing layer thickness and curing properties have significant effects on the photopolymerized structure and hence the mechanical properties. The appropriate curing process settings for varied particle loading fractions were analyzed and

identified in section 2, and were used to print samples in this study. To investigate the effect of layer thickness on mechanical properties of printed composites, S1-0 samples were printed with a 4.5% particle volume loading fraction and layer thicknesses of 30, 60, 80, 100, 120 and 150 μm. The corresponding curing time used for printing samples is 15, 18, 21, 23, 25 and 28s, respectively. Tensile tests as described in section 2.6 were performed on these samples. Table 1 shows breaking edges of samples after test.

It can be seen that the layer thickness has a slight effect on the Young's modulus, as shown in Fig. 11(e). However, the break propagation path changes significantly as the layer thickness increases. While the breaking propagation path is smooth for composites fabricated with thinner layers (30–60 μm), it becomes irregular with asymmetrical fractures for composites printed with thicker layers (80–150 μm). One reason for this asymmetrical break propagation path is probably be the micro-voids between layers in the 3D printed composites. When the layer thickness is large, micro voids are likely to be formed due to the poor interface between particle chains and polymer matrix.

Fig. 11(a–d) shows cross-sectional microscopic images with layer morphology in printed samples before and after mechanical test. Fig. 11 (a) and (b) show thin (30 μm) and thick (150 μm) layers in the 3D printed parts, respectively. We can observe that for thin printing layer (30 μm), the layer by layer accumulation occurs in a stable manner on the platform. But when the thickness is increased, larger number of agglomerated molecules are formed further away from the platform base layer. This causes a number of surface defects such as micro-gaps and micro-voids in adjacent surface layers. Such a micro-void is shown in Fig. 11(b). This kind of voids weakens the binding between adjacent layers and the interface between particle chain and polymer, leading to an irregular fracture. Fig. 11(c) and (d) show the cross-sectional area of break propagation paths of composites printed with thin (30 μm) and thick (150 μm) layers, respectively. For parts printed with thick (150 μm) layers (Fig. 11(d)), it can be seen that the micro-voids facilitate the cracks along the breaking edge.
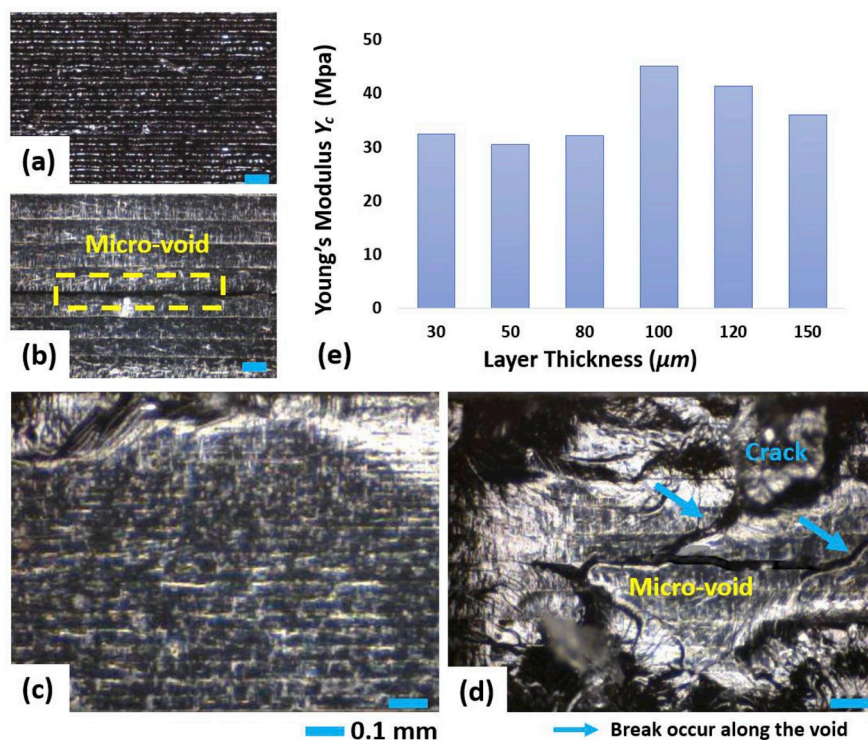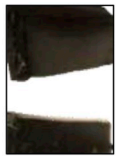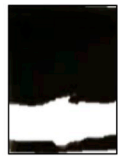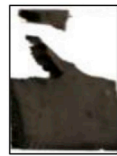

Fig. 11. Cross-sectional microscopic image of layers in printed parts before (a, b) and after (c, d) the mechanical test. (a, c) Correspond to the sample printed with thin layers (30 μm) and (b, d) correspond to the sample printed with thick layers (150 μm). (e) Relationship of Young's modulus with the printing layer thickness ($\varphi = 4.5\%$).

Table 1
Breaking edges of S1-0 samples printed with different layer thicknesses.

Layer thickness (μm)	30	60	80	100	120	150
Breaking Edges						

5mm

4. Conclusion

In this study, we investigated the influences of spherical particle chain orientations, volume loading fractions, and 3D printing layer thickness on the stress-strain behavior of 3D printed heterogeneous particle-polymer composites. We conducted mechanical tests and investigated analytical models, to understand how the elastic behavior of the polymer composites corresponds to distribution and orientation of spherical particle assemblies in polymer matrix.

This study gives us insight towards designing and 3D printing complex particle-polymer composites with programmable fracture strength and elastic properties. It is observed that the influence of 3D printing layer thickness on Young's modulus is negligible. However, the printing layer thickness parameter has some effects on the breaking propagation path due to the internal structure defects associated with large printing layer thickness. In our study, with a particle diameter of 300 nm and particle chain width of 5 μm, a 3D printing layer thickness smaller than 80 μm produce composites with smooth breaking edges. Whereas for composites printed with a larger layer thickness in this study, irregular breaking paths with asymmetrical fractures are usually observed, possibly due to micro-voids present between layers in the 3D printed composite part. How to determine this critical value of printing layer thickness for composites with different materials and printed by different processes, is still an open question and can be a topic for future research.

With extensive analytical and experimental investigation, we can conclude that, to achieve enhanced mechanical properties with reinforced architecture for a 3D printed assembled spherical particle-polymer composite, the sample should have a high particle loading fraction and parallel particle chain orientation. This study also showed that the Cox-Krenchel model with Carman-Reifsnider correction can also be applied to 3D printed particle chain-polymer composites, which are fabricated in a layer-by-layer fashion. It is the first experimental validation of this model on composites composed of polymer matrix and spherical particle chains. The model predicts a bigger Young's modulus of S1-0 samples than the actual ones, due to treating the particle chain as fibers directly. On the contrary, the Young's modulus of S1-90 samples predicted by the model are significantly smaller than experimental results, because the actual particle chain-polymer interface bonding is weaker than the assumption in the model.

This study of mechanical characteristics of particle-polymer composites offers new fundamental knowledge to design and additively manufacture polymer composites with assembled spherical particle chains for applications in mechanical, industrial and bioengineering field.

Author disclosure statements

No competing financial interests exist.

Acknowledgement

References

[1] Wegst UG, Bai H, Saiz E, Tomsia AP, Ritchie RO. Bioinspired structural materials. Nat Mater 2015;14(1):23.
[2] Yang Y, Chen Z, Song X, Zhang Z, Zhang J, Shung KK, et al. Biomimetic anisotropic reinforcement architectures by electrically assisted nanocomposite 3D printing. Adv Mater 2017;29(11).
[3] Studart AR. Additive manufacturing of biologically-inspired materials. Chem Soc Rev 2016;45(2):359–76.
[4] Yang Y, Song X, Li X, Chen Z, Zhou C, Zhou Q, et al. Recent progress in biomimetic additive manufacturing technology: from materials to functional structures. Adv Mater 2018;30(36). 1706539.
[5] Yang Y, Li X, Zheng X, Chen Z, Zhou Q, Chen Y. 3D-Printed biomimetic super-hydrophobic structure for microdroplet manipulation and oil/water separation. Adv Mater 2018;30(9). 1704912.
[6] Lu L, Joyee EB, Pan Y. Correlation between microscale magnetic particle distribution and magnetic-field-responsive performance of three-dimensional printed composites. J Micro Nano-Manufacturing 2018;6(1):010904.
[7] Lu L, Guo P, Pan Y. Magnetic-field-assisted projection stereolithography for three-dimensional printing of smart structures. J Manuf Sci Eng 2017;139(7):071008.
[8] Hussain F, Hojjati M, Okamoto M, Gorga RE. Polymer-matrix nanocomposites, processing, manufacturing, and application: an overview. J Compos Mater 2006;40(17):1511–75.
[9] Advani SG, Hsiao K-T. Manufacturing techniques for polymer matrix composites (PMCs). Elsevier; 2012.
[10] Filipcsei G, Csetneki I, Szilágyi A, Zrínyi M. Magnetic field-responsive smart polymer composites. In: Oligomers-polymer composites-molecular imprinting. Springer; 2007. p. 137–89.
[11] Mostafaei A, Kimes KA, Stevens EL, Toman J, Krimer YL, Ullakko K, et al. Microstructural evolution and magnetic properties of binder jet additive manufactured Ni-Mn-Ga magnetic shape memory alloy foam. Acta Mater 2017;131:482–90.
[12] Gu D, Meiners W, Wissenbach K, Poprawe R. Laser additive manufacturing of metallic components: materials, processes and mechanisms. Int Mater Rev 2012;57(3):133–64.
[13] Frazier WE. Metal additive manufacturing: a review. J Mater Eng Perform 2014;23(6):1917–28.
[14] Pan Y, Patil A, Guo P, Zhou C. A novel projection based electro-stereolithography (PES) process for production of 3D polymer-particle composite objects. Rapid Prototyp J 2017;23(2):236–45.
[15] Lu L, Tang X, Hu S, Pan Y. Acoustic field-assisted particle patterning for smart polymer composite fabrication in stereolithography. 3D Print Addit Manuf 2018;5(2):151–9.
[16] Wang X, Jiang M, Zhou Z, Gou J, Hui D. 3D printing of polymer matrix composites: a review and prospective. Compos B Eng 2017;110:442–58.
[17] Boczkowska A, Awietjan SF, Pietrzko S, Kurzydłowski KJ. Mechanical properties of magnetorheological elastomers under shear deformation. Compos B Eng 2012;43(2):636–40.
[18] Kumar V, Lee DJ. Studies of nanocomposites based on carbon nanomaterials and RTV silicone rubber. J Appl Polym Sci 2017;134(4).
[19] Martin JJ, Fiore BE, Erb RM. Designing bioinspired composite reinforcement architectures via 3D magnetic printing. Nat Commun 2015;6. 8641.
[20] Danas K, Kankanala S, Triantafyllidis N. Experiments and modeling of iron-particle-filled magnetorheological elastomers. J Mech Phys Solids 2012;60(1):120–38.
[21] Jolly MR, Carlson JD, Munoz BC. A model of the behaviour of magnetorheological materials. Smart Mater Struct 1996;5(5):607.
[22] Zhou G, Jiang Z. Deformation in magnetorheological elastomer and elastomer–ferromagnet composite driven by a magnetic field. Smart Mater Struct 2004;13(2):309.

[23] Jolly M, Jolly MR, Carlson JD, Munoz BC, Bullions TJ. J. Intell. Mater. Syst 1996;7: 613. J Intell Mater Syst. 1996;7:613.

[24] Han Y, Mohla A, Huang X, Hong W, Faidley LE. Magnetostriction and field stiffening of magneto-active elastomers. International Journal of Applied Mechanics 2015;7(01). 1550001.

[25] Guan X, Dong X, Ou J. Magnetostrictive effect of magnetorheological elastomer. J Magn Magn Mater 2008;320(3–4):158–63.

[26] Ginder J, Clark S, Schlotter W, Nichols M. MAGNETOSTRICTIVE PHENOMENA IN MAGNETORHEOLOGICAL ELASTOMERS. Electrorheological Fluids And Magnetorheological Suspensions: World Scientific 2002:472–8.

[27] Galipeau E, Castañeda PP. A finite-strain constitutive model for magnetorheological elastomers: magnetic torques and fiber rotations. J Mech Phys Solids 2013;61(4):1065–90.

[28] Borin DY, Stepanov G, Odenbach S. Tuning the tensile modulus of magnetorheological elastomers with magnetically hard powder. J Phys Conf Ser 2013:012040. IOP Publishing.

[29] Varga Z, Filipcsei G, Zrínyi M. Magnetic field sensitive functional elastomers with tuneable elastic modulus. Polymer 2006;47(1):227–33.

[30] Farshad M, Benine A. Magnetoactive elastomer composites. Polym Test 2004;23 (3):347–53.

[31] Kumar V, Lee D-J. Iron particle and anisotropic effects on mechanical properties of magneto-sensitive elastomers. J Magn Magn Mater 2017;441:105–12.

[32] Gonçalves EM, Oliveira FJ, Silva RF, Neto MA, Fernandes MH, Amaral M, et al. Three-dimensional printed PCL-hydroxyapatite scaffolds filled with CNTs for bone cell growth stimulation. J Biomed Mater Res B Appl Biomater 2016;104(6):1210–9.

[33] Sanjay M, Arpitha G, Yogesha B. Study on mechanical properties of natural-glass fibre reinforced polymer hybrid composites: a review. Mater Today: proceedings 2015;2(4–5):2959–67.

[34] Wichmann MH, Sumfleth J, Gojny FH, Quaresimin M, Fiedler B, Schulte K. Glass-fibre-reinforced composites with enhanced mechanical and electrical properties–benefits and limitations of a nanoparticle modified matrix. Eng Fract Mech 2006;73(16):2346–59.

[35] Cremer P, Löwen H, Menzel AM. Tailoring superelasticity of soft magnetic materials. Appl Phys Lett 2015;107(17). 171903.

[36] Han Y, Hong W, Faidley LE. Field-stiffening effect of magneto-rheological elastomers. Int J Solids Struct 2013;50(14–15):2281–8.

[37] Ivaneyko D, Toshchevikov V, Saphiannikova M, Heinrich G. Effects of particle distribution on mechanical properties of magneto-sensitive elastomers in a homogeneous magnetic field. 2012. 12101401.

[38] Ivaneyko D, Toshchevikov V, Saphiannikova M, Heinrich G. Mechanical properties of magneto-sensitive elastomers: unification of the continuum-mechanics and microscopic theoretical approaches. Soft Matter 2014;10(13):2213–25.

[39] Keip MA, Rambausek M. A multiscale approach to the computational characterization of magnetorheological elastomers. Int J Numer Methods Eng 2016;107(4):338–60.

[40] Pessot G, Cremer P, Borin DY, Odenbach S, Löwen H, Menzel AM. Structural control of elastic moduli in ferrogels and the importance of non-affine deformations. J Chem Phys 2014;141(12):015005.

[41] Spieler C, Kästner M, Goldmann J, Brummund J, Ulbricht V. XFEM modeling and homogenization of magnetoactive composites. Acta Mech 2013;224(11):2453–69.

[42] Kalina KA, Metsch P, Kästner M. Microscale modeling and simulation of magnetorheological elastomers at finite strains: a study on the influence of mechanical preloads. Int J Solids Struct 2016;102:286–96.

[43] Joyee EB, Pan Y. A fully three-dimensional printed inchworm-inspired soft robot with magnetic actuation. Soft Robot 2019. http://doi.org/10.1089/soro.2018. 0082.

[44] Yunus DE, Shi W, Sohrabi S, Liu Y. Shear induced alignment of short nanofibers in 3D printed polymer composites. Nanotechnology 2016;27(49). 495302.

[45] Griffith ML, Halloran JW. Freeform fabrication of ceramics via stereolithography. J Am Ceram Soc 1996;79(10):2601–8.

[46] Pan Y, Dagli C. Dynamic resolution control in a laser projection-based stereolithography system. Rapid Prototyp J 2017;23(1):190–200.

[47] Pan Y, Chen Y. Smooth surface fabrication based on controlled meniscus and cure depth in microstereolithography. J Micro Nano-Manufacturing 2015;3(3):031001.

[48] Querry MR. Optical constants. MISSOURI UNIV-KANSAS CITY; 1985.

[49] Chartier T, Chaput C, Doreau F, Loiseau M. Stereolithography of structural complex ceramic parts. J Mater Sci 2002;37(15):3141–7.

[50] Jacobs PF. Rapid prototyping & manufacturing: fundamentals of stereolithography. Society of Manufacturing Engineers; 1992.

[51] Zhou W, Li D, Chen Z. The influence of ingredients of silica suspensions and laser exposure on UV curing behavior of aqueous ceramic suspensions in stereolithography. Int J Adv Manuf Technol 2011;52(5–8):575–82.

[52] Coleman JN, Khan U, Blau WJ, Gun'ko YK. Small but strong: a review of the mechanical properties of carbon nanotube–polymer composites. Carbon 2006;44 (9):1624–52.

[53] Ouglova A, Berthaud Y, François M, Foct F. Mechanical properties of an iron oxide formed by corrosion in reinforced concrete structures. Corros Sci 2006;48(12): 3988–4000.